Background-Oriented Schlieren Imaging of Supersonic Aircraft in Flight

James T. Heineck*
NASA Ames Research Center, Moffett Field, California 94035
Daniel W. Banks†
NASA Neil A. Armstrong Flight Research Center, Edwards, California 93523
Nathanial T. Smith‡
AerospaceComputing, Inc., Mountain View, California 94043
Edward T. Schairer§
NASA Ames Research Center, Moffett Field, California 94035
and
Paul S. Bean¶ and Troy Robillos**
NASA Neil A. Armstrong Flight Research Center, Edwards, California 93523

This paper describes the development and use of background-oriented schlieren imaging of a full-scale supersonic jet in flight. A series of flight tests was performed in April 2011, October 2014, February 2015, and December 2018 using the flora of the desert floor in the supersonic flight corridor near the Edwards Air Force Base as a background. Flight planning was designed based on the camera resolution, the mean size and color of the predominant plants, and coordination of several aircraft. Image processing was done with both cross correlation and optical flow algorithms. The planning proved to be effective, and the vast majority of the passes of the target aircraft were successfully recorded. Results were obtained that are the most detailed schlieren imagery of an aircraft in flight to date.

Nomenclature

D_n = vector sum of the defection at angle n, pixels
D_x = ray deflection in the image-space horizontal direction, pixels
D_y = ray deflection in the image-space vertical direction, pixels
I = image intensity, in grayscale
i = x coordinate of image processing grid node
j = y coordinate of image processing grid node
M = Mach number
u = D_x displacement, in pixels, used in the optical flow equations
v_y = D_y displacement, in pixels, used in the optical flow equations
α = weighting term for smoothing penalty in the optical flow equations
Δx = horizontal registration shift of the reference image to the data image, pixels
Δy = vertical registration shift of the reference image to the data image, pixels

*Physical Scientist, Experimental Aero-Physics Branch; james.t.heineck@nasa.gov. Senior Member AIAA.
†Aerospace Engineer, Aerodynamics and Propulsion Branch. Associate Fellow AIAA.
‡Research Engineer, Experimental Aero-Physics Branch. Member AIAA.
§Aerospace Engineer, Experimental Aero-Physics Branch. Member AIAA.
¶Aerospace Engineer, Advanced System Development Branch.
**Aerospace Engineer, Flight Instrumentation and Systems Integration Branch.
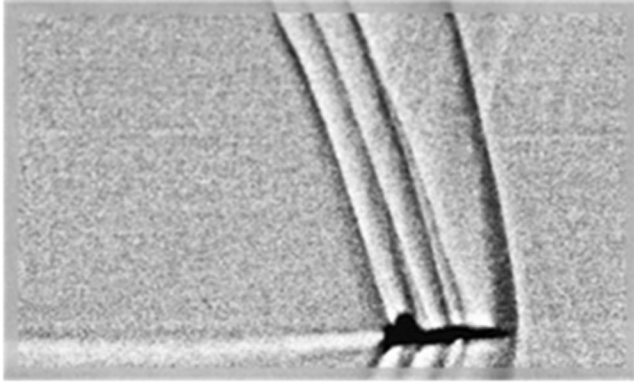
I. Introduction

HISTORICALLY, obtaining schlieren images of refractive index gradients caused by fluid density gradients required mirrors or lenses to collimate a spherically radiating light source that passes through the field of interest. That collimated beam is refocused so that a knife edge can be positioned to cutoff a portion of the crossing rays, which act to both increase the sensitivity of the system and render the first derivative of the gradient normal to that knife edge. That conditioned beam is then photographically recorded. Settles [1] offers a comprehensive review and practical guide to the art and science of density gradient imaging. However, practice has shown that there are advantages and pitfalls to nearly all of the techniques he describes. No one method will ever fit all situations. Mirror or lens optics can achieve the highest sensitivity but limit the size of aerodynamic investigations. Retroreflective screen shadowgraphy is not limited by mirror or lens optics but renders only the second derivative of the refractive index of the density gradient. Retroreflective focusing schlieren achieves both size and sensitivity but can be severely affected by high vibration environments and is difficult to set up. With the invention of synthetic schlieren in 1998 by Dalziel et al. [2] and subsequent improvements and renaming the technique to background-oriented schlieren in 1999 to 2000 at DLR, German Aerospace Center Göttingen [3,4], those field-of-view limitations were removed and high sensitivity is achievable with simple optics. All that is required is a digital camera, either still or video, and a suitably textured background that lends itself to image cross correlation or optical flow image processing. While this seems to be a candidate method for all density gradient imaging applications, the method requires careful system design and intensive postprocessing; and it is well suited for large-area applications where an appropriate background can be created or a natural background can be exploited. It is a choice for experiments where optical access does not permit conventional schlieren methods. It is also a method that easily accommodates multicamera applications such as stereoscopic or tomographic imaging.

A systematic approach to obtaining schlieren imagery of an aircraft in flight began with Weinstein [5], whose telescopic imaging of the sun limb provided a "knife edge" to produce the schlieren effect. This technique requires the aircraft to be flown precisely between the observing telescope system on the ground and the sun, which

Fig. 1 Weinstein's in-flight schlieren image of a supersonic aircraft from 1994 [5].

subtends an angle of 1/2 deg. This film-based streak camera method observed and recorded the distortion of the outer edge of the sun limb. The cumulated image sequence of the distorted sun edge was processed to provide a schlieren image. His results are widely recognized as a milestone in flight testing (Fig. 1).

NASA Aeronautics' Commercial Supersonics Technology Project has been developing new aircraft designs that reduce the downward-propagating shock waves, or sonic boom. The culmination of this program is the X59 Quiet Supersonic Technology (QueSST) Low-Boom Flight Demonstrator. The need for visualizing the shock waves generated by this aircraft has prompted the development of schlieren imaging methods for the flight testing. Three methods are being developed in parallel, each complimentary to the other. Two methods, the ground-to-air schlieren photography system and the background-oriented schlieren with celestial objects (BOSCO) [6], use ground-based telescopes that image the sun as an aircraft passes between the sun and telescope; and they are direct outgrowths of Weinstein's pioneering method [5]. A third method, the air-to-air background-oriented schlieren (AIRBOS), images the target aircraft from an observation aircraft flying above it and uses the natural flora on the ground to derive the schlieren imagery. The sparse Mojave Desert flora of the Black Mountain Supersonic Corridor near Edwards Air Force Base provides a nearly ideal background for this technique. This method was first demonstrated in April 2011 [7], although the publication has restricted release.

This air-to-air method is an extension of the background-oriented schlieren (BOS) method described by Richard and Raffel [3]. In 2000, Raffel et al. demonstrated the use of background-oriented schlieren as a method to show wingtip and rotor vortices for full-scale aircraft [4]. The technique proved to be effective, and they subsequently performed

flight tests in Germany using leaves of the forest in the Harz Mountains as their background [8]. In 2012, the DLR, German Aerospace Göttingen group demonstrated the AIRBOS technique on full-scale helicopters in flight, rendering the blade-tip vortices and engine exhaust [8,9]. Additionally, Raffel et al. summarized a number of large-scale BOS experiments, which include an array of both ground-based and flight applications [10,11]. In the subsequent two decades since its invention, BOS has become widely used for applications. Tomographic reconstruction techniques have pushed BOS into three-dimensional rendering of density gradients and lead to the quantification of density and temperature. First suggested by Raffel et al. [4] but subsequently developed by a number of researchers worldwide [12–18], three-dimensional reconstructed density fields have become the ultimate manifestation of the BOS technique. Three-dimensional BOS has been a particularly useful measurement tool for the characterization of supersonic jets due to the relative ease of the optical setup in laboratories and test cells, as well as the ability to quantitatively derive density gradients [14,19,20].

II. BOS Technique

BOS works by detecting minute shifts of features in a visually textured background caused by the presence of a density gradient, which creates a refractive index change in the air (Fig. 2). A light ray from the background (a speckle) passes through a density gradient and is deflected. The angle of deflection ε is proportional to the strength and optical thickness of the gradient along the line of sight. The apparent shift in the location of a speckle pattern is detected with either image cross correlation or optical flow algorithms. The position of the correlation peak defines the shift: D_x and D_y. The "schlieren image" is a grayscale mapping of the displacement in x, y, some vector sum, or absolute magnitude. A properly designed BOS system will have the speckle size in the 2–5 pixel range [3]. A quiescent image of the background serves as a reference to the image of the background distorted by the density gradient.

These distortions are often smaller than a pixel, and so they are hard to detect with a naked eye. However, image processing techniques such as cross correlation and optical flow reveal these minute displacements of the speckle pattern. Figure 2 also shows the work flow and principle of BOS. As with all measurement techniques that use image cross correlation [e.g., particle image velocimetry and surface deformation measurements (sometimes known as digital image correlation)], the higher the resolution of the camera, the more detail can be gleaned. Cross-correlation detection algorithms comfortably detect displacements of less than one-tenth of a pixel. Thus, a sensor with small pixels (4–10 μm) will be more sensitive and able to detect weaker gradients that produce smaller background displacements than a sensor with larger pixels (20–25 μm) assuming the same lens.
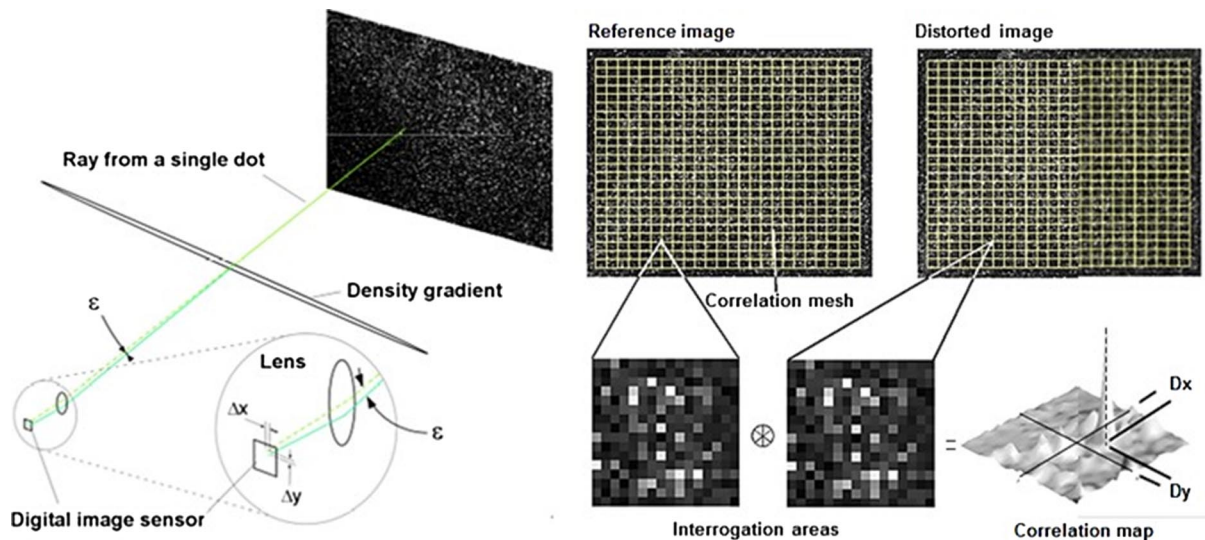
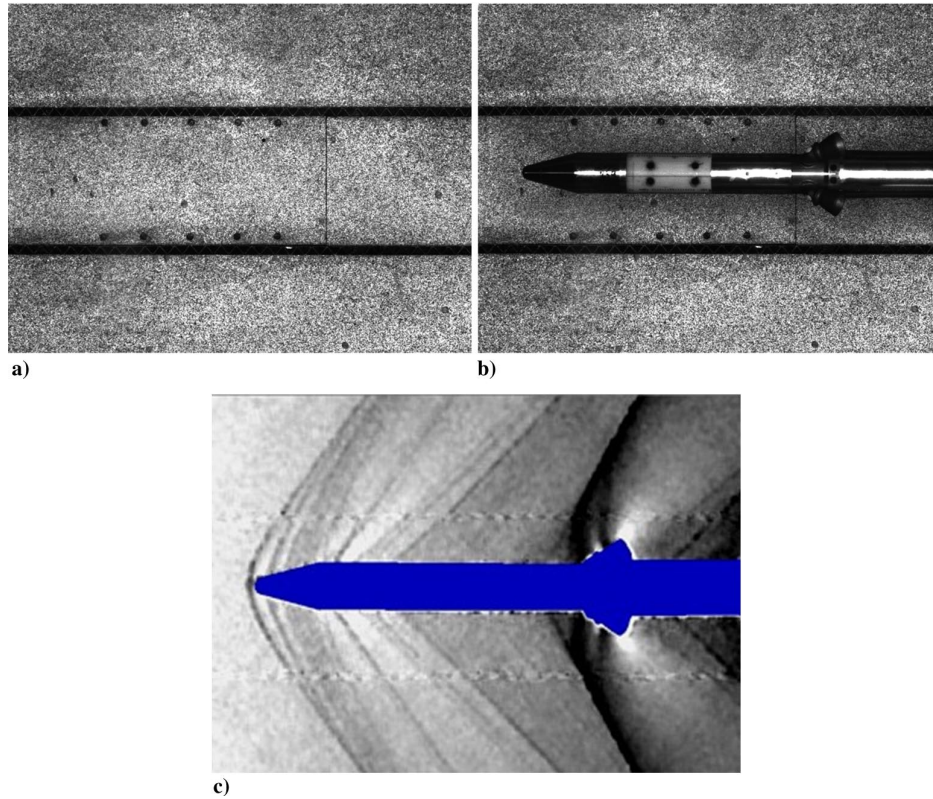

Fig. 2 Principle of BOS.

Fig. 3   Examples of BOS imagery from wind-tunnel testing.

The data that result from the cross correlation are an array of points with displacements in the horizontal $x(D_x)$ and vertical $y(D_y)$ directions in the image plane proportional to the density gradient. Assigning a gray level proportional to D_x and D_y or a vector sum of D_x and D_y, and rendering the data as a contour plot, results in an image that is analogous to conventional schlieren imagery. A plot of D_x is equivalent to a vertical knife orientation, a plot of (D_y) corresponds to a horizontal knife orientation, and a plot of D_n corresponds to the gradient normal to the angle of the vector sum.

Figure 3 is an example of wind-tunnel imaging using retroreflective background-oriented schlieren [21] applied to the NASA Ames Research Center's unitary plan 11 ft transonic wind tunnel. In this figure are the reference (Fig. 3a), wind-on (Fig. 3b), and processed schlieren images (Fig. 3c) of the launch abort tower of the Orion Space Capsule in Mach 1.3 flow. The schlieren image is a contour plot of the horizontal deflection distances (in pixels.) The background was made by careful sputtering of retroreflective paint on the floor of the tunnel and imaging that background with a digital camera. The first image (Fig. 3a) was acquired without the presence of the model, and it acts as the reference (wind off), the second image (Fig. 3b) is the data image (wind on), and the third (Fig. 3c) is the result of displacements computed by cross correlation of the reference (wind off) and data (wind on) images. This image shows D_x displacements for a launch abort tower in Mach = 1.3 flow. Here, the compression waves are dark and the expansion fans are light.

III.   Flight Planning: Making AIRBOS Work

The approach to applying this technique to flight was to observe and record the supersonic aircraft flying under a slower-moving aircraft. The sparse desert flora is used as the visually textured background. The optical system and flight planning were designed to optimize the parameters of the BOS technique. Of particular importance was the size of the background speckles in the image of the camera. Speckle size is dependent on the physical size of the flora, the lens focal length, the camera pixel size, and the altitude. The angular field of view is dependent on the sensor size. The dominant plant that can be seen from high altitude in the Mojave Desert is the creosote

bush, interspersed with Joshua trees. The Joshua trees were not in sufficient abundance in the target area to factor in the average size of the flora, and so the attention was focused on the creosote bush. There are three special characteristics of the creosote plant in this environment. The first is that it grows to approximately 10–12 ft in diameter (3–4 m). Second, creosote emits a natural herbicide that maintains separation of 5–10 ft (1.5 to 2 m) between plants to prevent overpopulation in an arid landscape [22]. Third, the contrast can be enhanced using a red filter, making the creosote plants appear much darker than the desert floor. Taken together, these characteristics make creosote bushes an excellent speckle in the background for implementing the AIRBOS technique (see the desert floor in Fig. 4).

The flight configuration consisted of a slow-moving observation aircraft, which was the NASA Super King Air (B200), flying at one altitude with the supersonic test aircraft, which was the Air Force T-38, flying at a lower altitude directly below the observer. Figure 5 shows in-flight photographs of each aircraft. The flight plan sought to have the target aircraft as high as practical. While the service ceiling of the King Air is 35,000 ft above mean sea level, operationally, 30,000 ft was more time efficient and still allowed for higher-altitude supersonic passes where higher Mach Numbers are more easily achieved. The cameras in the King Air were mounted in a windowed nadir-view port. So, with altitude, sensor, and speckle dimensions defined, a lens was chosen that rendered the background at the desired spatial resolution (2–5 pixels/bush). Reference images were acquired by the observer aircraft before the test aircraft entering the camera field of view, thus continuous recording was necessary as the test aircraft approached.

The imaging system consisted of two Phantom V641 cameras, whose sensors were 2560×1600 pixels with a 10 μm pixel pitch. Their maximum full-frame recording frequency is 1470 frames per second. The integration times for each exposure ranged between 50 and 80 μs, depending on lighting conditions. This effectively eliminated motion blur. The frame rate was changed for each pass, depending on separation distance. The resolution of the bushes is an important parameter to optimize; so, this was established by the altitude and the approximate average diameter of a creosote bush. An Excel worksheet was created that calculated the resolution and
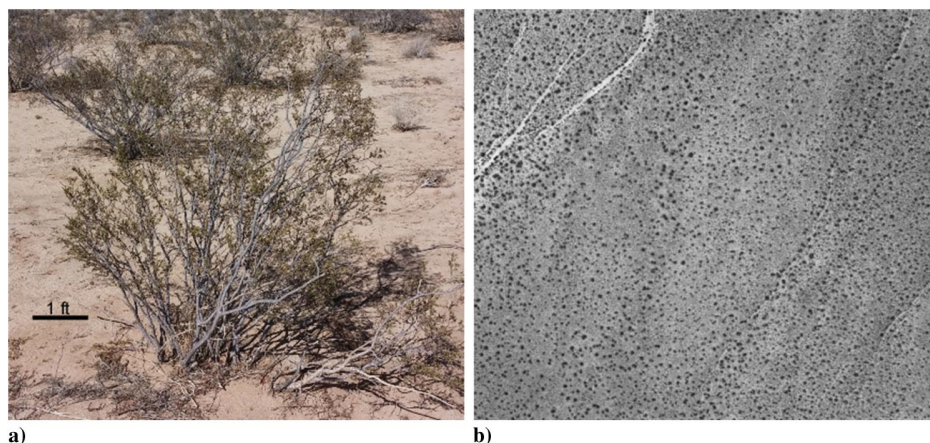
Fig. 4   Photographs of a) creosote bush found in the Mojave Desert, and b) sample of the desert floor acquired with the imaging system.
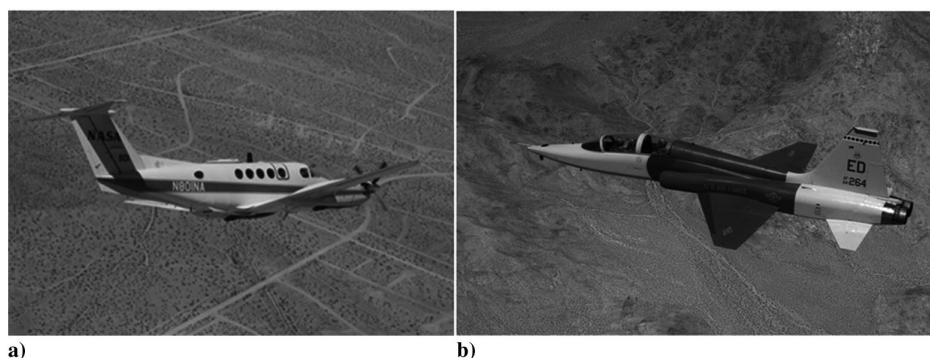

Fig. 5   Photographs of a) Beechcraft B-200 Super King Air observing aircraft, and b) U.S. Air Force T-38 target aircraft.

angular fields of view for different combinations of camera and lens parameters and aircraft altitudes. Since the average bush diameter was determined to be 10–12 ft and the observer altitude was 30,000 ft, the appropriate lens focal length was deterministic. A 180 mm lens was chosen, giving an 8 deg field of view.

The sensor spectral response is quasi parabolic between 350 and 950 nm, and it peaks at 640 nm with approximately 55% quantum efficiency at that wavelength [23]. A no. 25 red glass filter was attached to each lens to improve contrast and mitigate the effects of atmospheric haze. This long-pass filter blocks light 580 nm and shorter. By blocking some of the green light reflecting from the foliage, contrast is increased as the filter renders the bushes darker against the light-gray soil and dried grass. Figure 4 is a photograph of a typical creosote bush in the Mojave Desert as well as a view of the desert floor from near flight altitude.

Two nadir camera ports are available in the King Air. Figure 6 is a drawing of the cabin layout. The Phantom cameras were mounted to a common plate and bracketed to a flange plate that was adapted to the window structure. A legacy camera from the 2011 test campaign was mounted in the second port of the observation aircraft. This was a Goodrich SUI SU640-SDWHVis-1.7RT Indium Gallium Arsinide (InGaAs) camera with a 640×512 pixel sensor and 25 μm pixel pitch, and it was fitted with a 105 mm lens. It was used as a real-time spotting camera.

Figure 7 is a diagram of the flight pattern each aircraft followed over the supersonic corridor. The data acquisition began at the beginning of the straight run of the King Air over the target area of the supersonic corridor. The King Air pilot used an onboard Global Positioning System (GPS) unit to establish the course line. The T-38 aircraft used military-grade GPS for navigation.
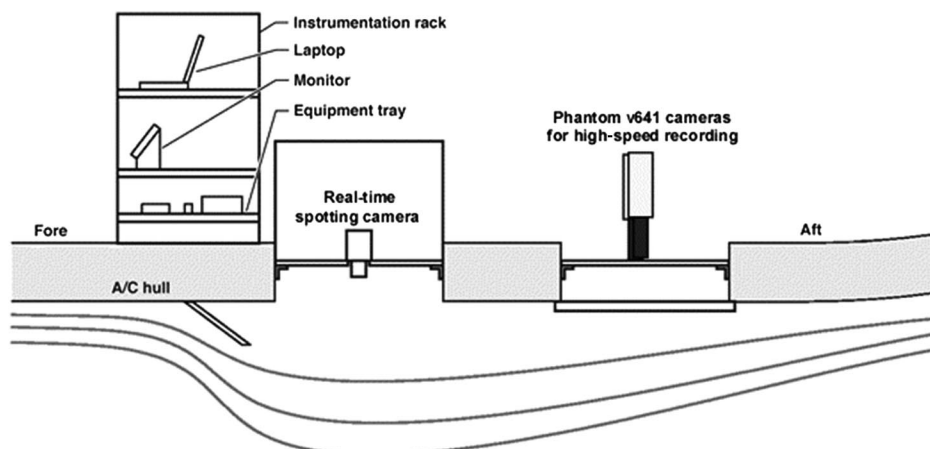

Fig. 6   Layout of imaging system in the aircraft hull (A/C hull) of the Beechcraft B-200 Super King Air observing aircraft for the second and third AIRBOS campaigns.
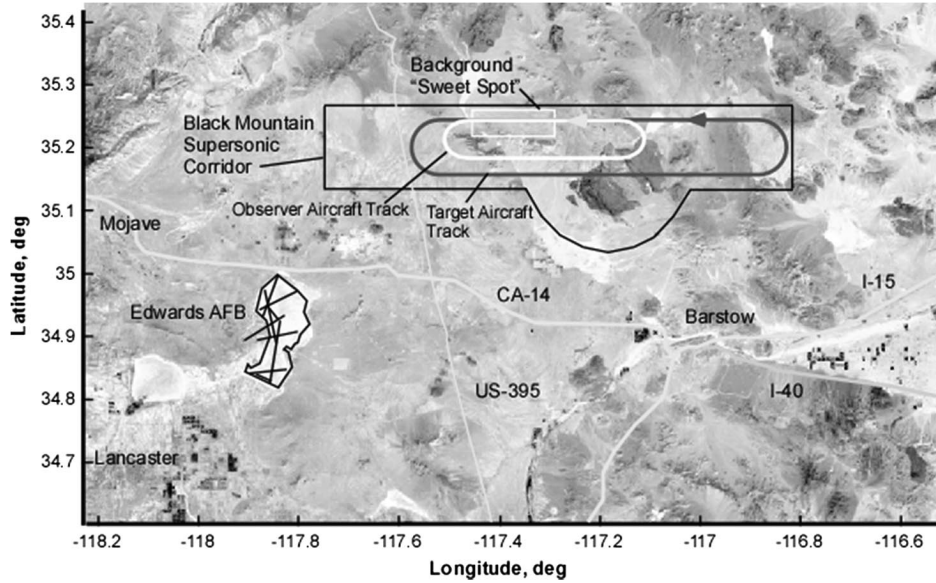
Fig. 7   Flight course line and reentry pattern of the King Air (observer) and the supersonic aircraft (target) in the Black Mountain Supersonic Corridor. Image from Google Earth.

A reconnaissance flight was made over the area of the corridor that appeared to be the best location for the BOS background. The area was quickly evaluated in Google Maps using satellite view and then imaged with the cameras during the flight for direct evaluation with the cross-correlation program. Hargather and Settles describe a method to evaluate natural backgrounds for the purpose of BOS applications [24]. This method was not required: the quality of the background was sufficient to allow for determining the minimum interrogation size that produced a signal-to-noise ratio (SNR) of four or greater by using a correlation function between two sequential images. As the interrogation area decreases, more detail can be gleaned. However, as the interrogation area decreases, the SNR decreases. A 16 pixel window size gave a SNR of 5.24, and so subsequent data were processed with this parameter.

IV.   Image Processing: Cross Correlation

Image processing algorithms were used to determine the pixel shift of the background. Pixel shift is a function of the change of index of refraction and the optical thickness of that index gradient. These data were processed using an in-house program called BOS_ETS. Several image processing steps were required to produce the schlieren image. The initial step was determining which of the numerous passes were the most appropriate to process: on some passes, the target aircraft did not enter the camera view; others were over areas of the desert with sparse plant density. A sequence, such as shown in Fig. 8, was extracted from each pass for processing. The first image of each sequence was the last "clear" frame. The stack of subsequent images was registered to the first using software developed at NASA Ames Research Center. This eliminated the effects of movement of the observer aircraft relative to the desert floor and assured that the displacements calculated were not offset by any apparent movement in the background.

A.   Reference Image Alignment

The displacement of the background in each image relative to the first image was measured by image cross correlation in a large interrogation window far removed from where the test aircraft appeared. The first time the images were analyzed during the 2011 campaign, they were registered using only a single interrogation window, resulting in simple x and y displacements of each image relative to the first. It was discovered, however, that this correction did not account for small variations in attitude of the observer aircraft. Therefore, as an alternative, each image was registered to the first image based on displacements measured at four reference points located near the

corners of the images, and a first-order projective transformation was computed:

$$x = \frac{a_1 x_0 + a_2 y_0 + a_3}{c_1 x_0 + c_2 y_0 + 1} \qquad (1a)$$

$$y = \frac{b_1 x_0 + b_2 y_0 + b_3}{c_1 x_0 + c_2 y_0 + 1} \qquad (1b)$$

where (x_0, y_0) and $(x = x_0 + D_x, y = y_0 + D_y)$ are the image coordinates of the reference points in the reference and the current image, respectively. The eight coefficients of the transformation $(a_{1-3}, b_{1-3}, c_{1-2})$ were determined by stacking equations for x and y at the four reference points and solving the resulting set of eight linear equations for the unknown coefficients. Then, the transformed pixel coordinates of each point in the current image were computed from Eqs. (1a) and (1b). This eliminated differences in the processed images that were not caused by the disturbances created by the flow features of the test aircraft. These differences include those due to pitch, roll, or yaw of the observer airplane, as well as camera and lens vibration. Without this registration method, each processed solution had large biases that required odious corrections to make the deflections.

B.   Reference-to-Data Image Correlation

Once the images are registered, local displacements of the background due to disturbances created by the test aircraft are determined by defining an interrogation grid and computing the displacement of each node by image cross correlation. The grid density was set to have a node every three pixels to achieve the highest-resolution schlieren image possible. Image cross correlation fails if the pixel displacements exceed half the interrogation window size. Therefore, a multigrid method was applied, starting with a 32×32 pixel window, and followed by a second pass with a 16×16 pixel window. A high-pass filter of 5×5 was applied before the correlation pass. A five-point Gaussian peak finder was applied in each direction to encompass the size of the plants after the high-pass filtering. Finally, a conservative outlier detection was performed, where outlier data were replaced by data interpolation.

The data from this correlation step produce an array dataset of i, j, D_x, D_y, and SNR for each correlation. The displacements of D_y were made into a grayscale contour plot to produce the final single-instance schlieren image. Figure 9 shows the results of cross correlation of the aligned reference image to the single images from the
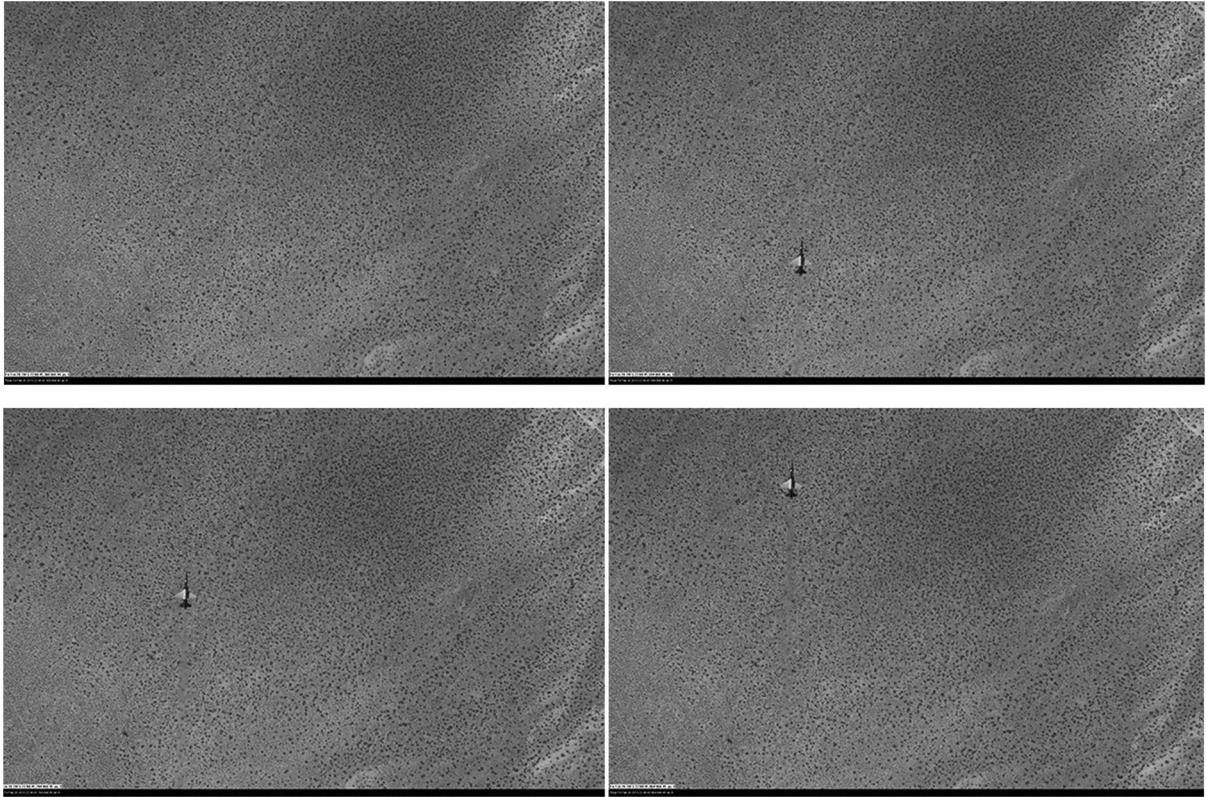
Fig. 8   Sequence of raw images selected from the series of 300+ acquired from a pass where the observer flew at 28,300 ft above ground level (AGL) and the test aircraft flew at 23,300 ft AGL.
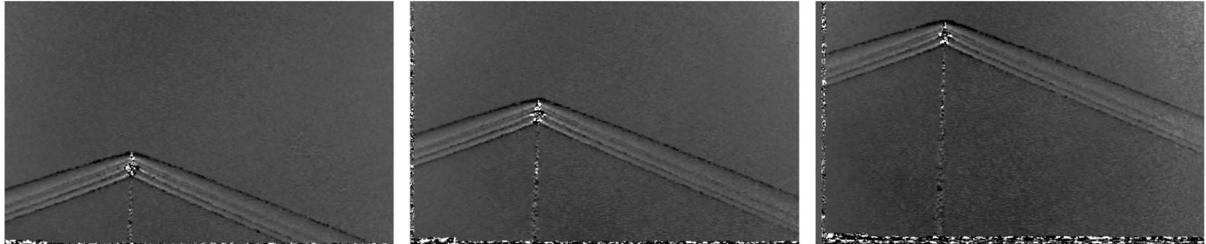

Fig. 9   BOS images of single frames from the sequence. Each image is a contour of the vertical deflection, D_y of ± 2 pixels. Note the slight change in tone as the sequence progressed. Target is flying at $M = 1.05$ and is 5000 ft below observer.

aforementioned sequence. There is an accumulated band of noise on the side and bottom of the images as the background from the data image moves further down course from the reference image. If the observer was perfectly stationary, this noise band would not be seen.

C.   Averaging of Schlieren Data

Random correlation noise always limits the BOS image quality. Supersonic wind-tunnel data consisting of multiple images of the same condition can be simply averaged since data images are registered to the reference and the model tends to be stationary. In the AIRBOS case, the target aircraft moves through the field of view such that a simple average of the sequence as it is processed is not applicable. A second tracking algorithm was written to account for the interframe motion of the target aircraft after the data image is registered to the reference image. This algorithm shifted the data grid to match the pixel displacement of the aircraft. The shift was determined by cross-correlating features on the aircraft, such as a specular highlight, after the registration step. The displacement data from each sequence are averaged, but not the grayscale images' output from the individual sequence plots. This permits plotting the averaged data in any "virtual" knife-edge angle, as well as the absolute magnitude of displacement (which is used to calculate density in tomographic BOS, but not the objective in this application). The image in Fig. 10 is an average of 150 instantaneous
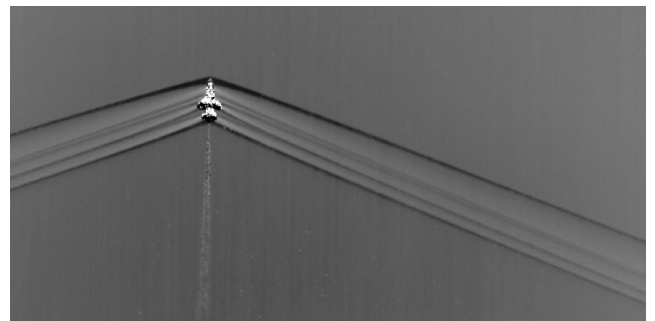

Fig. 10   A simple average of the resulting D_y data ± 2 pixels. An aircraft tracking utility in the BOS program allows for registering the correlation grid from each instance.

images and clearly shows the major shock structure generated by the aircraft, including the expansion fan around the canopy. One artifact of this averaging scheme is the streaks that result from inconsistent bush distribution, where sparse areas result in noisier correlations. The correlations of those sparse areas propagate as the plane passes through the image area. The errors show as streaks in the BOS image.

V. Effects of Separation Distance

Increasing the details in the shock structure was attempted by closing the separation distance between the observer and target aircraft. While this was desirable from an imaging perspective, the imaging cone narrows such that a separation distance of 2000 ft provides only a 200 ft cross-track window for the pilot to fly through. This makes the navigation more difficult. Also, the transit time of the aircraft in the camera field of view is reduced, requiring higher frame rates and careful trigger timing to assure that enough images per pass were acquired for sufficient averaging. Figure 11 demonstrates the improved detail for the shock structure resulting from increasing the magnification of the area of interest by reducing the separation distance. Note that changing the lens to a longer focal length would increase the size of the images of the bushes, and so separation distance is the only parameter available for increasing magnification.
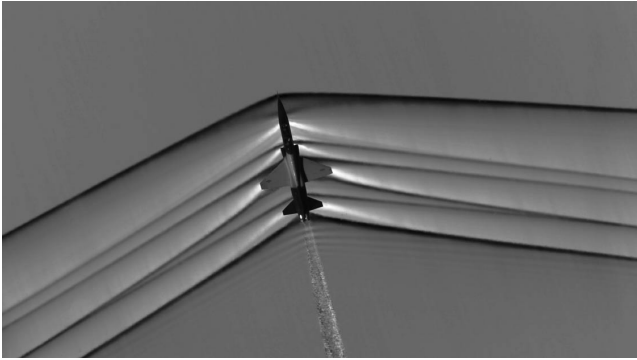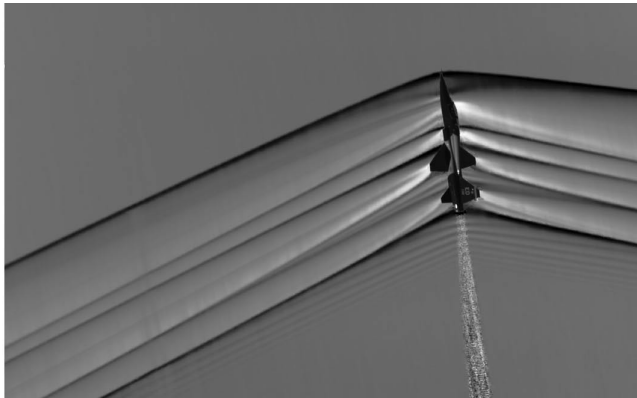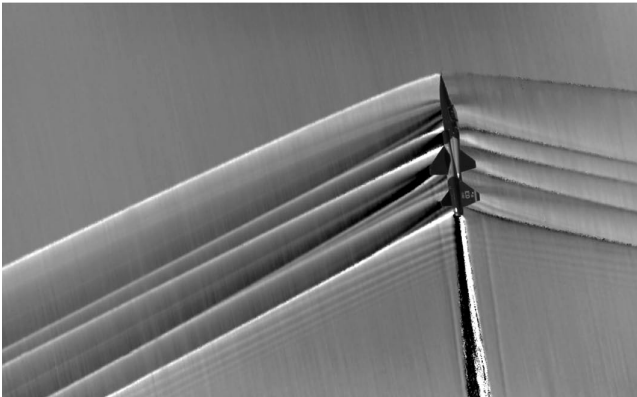

Fig. 11 Average of D_x in grayscale ± 2 pixel contour of the shock structures around the T-38 at $M = 1.05$.

a)

b)

Fig. 12 BOS image with aircraft of T-38 in 45 deg roll revealing shocks emanating from structures on underside of aircraft: a) contour of D_y value ± 2 pixels, and b) contour of D_x value ± 1 pixel.

Figure 12 shows a similarly processed image on a pass where the pilot attempted a 90 deg roll. The intent is to view the downward-propagating shocks that a person on the ground would experience. Unfortunately, the roll was only 45 deg but the downward-propagating shocks are visible. Figure 12a is a plot of ± 2 pixel deflections in the D_y direction; and Fig. 12b, produced from the same dataset, is a contour plot of ± 1 pixel lateral deflection D_x. Note that the wingtip vortices have been rendered in this view. The stronger appearance of the streaks due to correlation error in the average are attributed to the narrower grayscale, and so the noise is a higher percentage of the signal.

VI. Image Processing: Optical Flow

Optical flow methods are an alternative method to image cross correlation for measuring the background displacements in the images. The success of the BOSCO image processing using the Lucas–Kanade optical flow algorithm [25] by Hill and Hearing [6] prompted the authors to more fully investigate the suite of available optical flow methodologies. This is not the first application of optical flow to schlieren imaging. A compelling case for using optical flow in BOS applications was published by Atcheson et al. [26] in 2009. The use of optical flow for large-scale wind tunnel and flight testing are described in [6,27,28]. Hill's use of optical flow for the BOSCO technique was critical to the success of the method.

Optical flow, or the apparent motion between images due to brightness changes, is a well-established technique developed by the computer vision community for motion estimation in image pairs and video. Numerous algorithms exist for the calculation of optical flow, and they may be grossly classified as local or global methods. This work uses the global regularization based method of Horn and Schunck [28]. The Horn–Schunck method was selected due to both its ability to solve the flowfield at every image point and its successful implementation, as detailed in Ref. [26].

Optical flow has two major assumptions: the brightness of an object or pixel remains constant through the sequence, and the motion of an object between frames is small. The assumptions used to derive the brightness constancy equation (or brightness constraint) are given by

$$I_x u + I_y v = -I_t \qquad (2)$$

where I is the local image intensity, in gray values; u and v are the two-dimensional displacement components; and the subscripts denote the spatial and temporal derivatives. An additional constraint is required to solve Eq. (2) completely. It is assumed that nearby points have similar motions, and that the velocity changes are smooth within a neighborhood. This is referred to as the smoothness constraint, represented by expression (3):

$$\left(\frac{\partial u}{\partial x}\right)^2 + \left(\frac{\partial u}{\partial y}\right)^2 + \left(\frac{\partial v}{\partial x}\right)^2 + \left(\frac{\partial v}{\partial y}\right)^2 \qquad (3)$$

The brightness constancy constraint and the smoothness constraint can be combined to form a function that can be minimized over a domain. This creates a regularization problem over the image in expression (4):

$$\iint \left\{ (I_x u + I_y v + I_t)^2 + \alpha^2 (\|\nabla u\|^2 + \|\nabla v\|^2) \right\} \mathrm{d}x\mathrm{d}y \qquad (4)$$

where α is the weighting term for smoothing penalty. The goal is to minimize the function in expression (4) such that the total error, which is the sum of the brightness constancy and the smoothness errors, approaches zero.

Significant noise reduction in the single BOS solutions was achieved by using a multireference technique, where several images in the sequence before the aircraft entry into the frame were used to create separate, independent solutions [27]. This technique was developed specifically for these data since the method of acquiring many frames before aircraft frame entry lent itself to straightforward implementation. Each reference image rendered the undisturbed
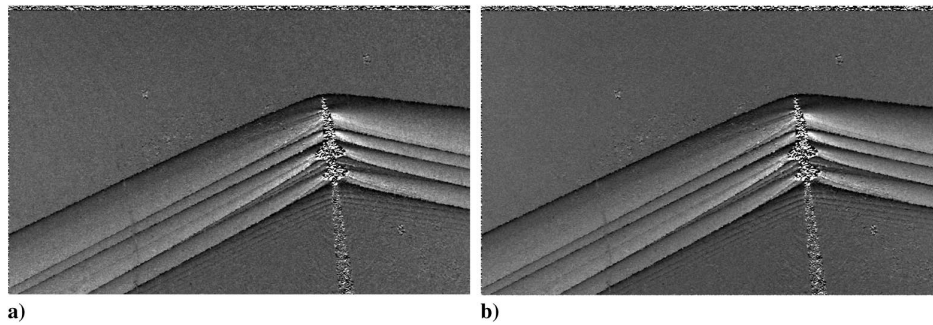
Fig. 13   Example single data image processed using a) a single reference frame and b) 10 reference frames then averaged. Note the Moire pattern in the single-reference image has been eliminated in the multireferenced image.

background with pixel-level differences in the pixel aliasing of each speckle feature. Since optical flow calculates a solution pixel by pixel, the random noise of the solutions is different for each reference background and tends to cancel out with subsequent averaging, revealing more detail in unsteady features such as the Mach wave radiation emanating from the plume. This technique was found to be less effective when originally applied to the cross-correlation solutions; although, some improvement was seen when the interrogation window got smaller. Figure 13 shows two solutions of the same data frame. Figure 13a uses a single reference, and Fig. 13b is an average of 10 solutions from 10 different reference frames. Note the reduction of granularity of the noise, the elimination of the Moire pattern, as well as the enhanced rendering of Mach wave radiation.

Figure 14 is a plot of the SNR of the signal vs the number of reference. The two lines are from two different flight passes, adding credence to the theory that multireferencing actually reduces the noise of a single data image optical flow solution.

Figure 15 is a result using this algorithm on the same raw images used to make the images in Fig. 12. Each of the instantaneous images were processed with 10 reference images from the image data sequence and then averaged. This multireference technique did not significantly improve the cross-correlation results. However, due to the slightly different pixel aliasing of the details of the reference background images at a pixel level, the optical flow noise improved significantly. Then, as was done with the cross-correlation solutions, approximately 200 of these instantaneous solutions were realigned to the plane's coordinates and then averaged, yielding the highest-fidelity in-flight schlieren image to date.

Figure 16 shows a comparison of the results from cross correlation (Fig. 16a) and the Horn–Schunck algorithm (Fig. 16b). Each result is the product of averaging 200 instantaneous solutions and in contour of ± 2 pixels. The improved detail in the optical flow solution can be
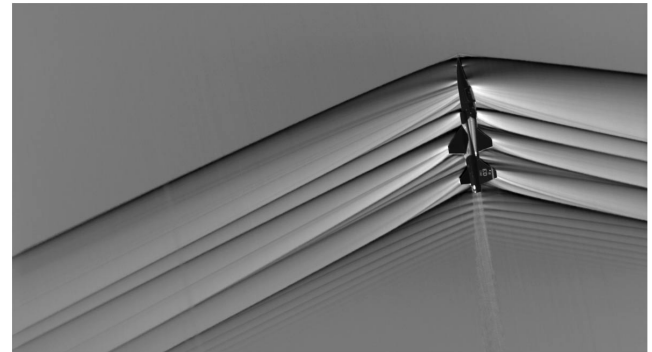

Fig. 15   Contour of ± 2 pixels in the D_y direction from optical flow method using the same raw image data as were used for Fig. 12 (original image of plane added after processing).

attributed to the resolution of the two solution arrays: the cross-correlation interrogation grid is one-quarter of the window size (in this case, 16 pixels). Thus, the grid nodes are at a four-pixel interval, making the BOS solution one-quarter of the resolution of the per-pixel optical flow solution. Note the increased detail in the expansion fans around the canopy and wingtips, as well as the weak shock from the nose probe.

VII.   AIRBOS4 Campaign

In December of 2018, a fourth flight campaign was conducted where a new camera configuration and data acquisition system were integrated on the B-200 King Air. Three Phantom V641 cameras were mounted in the downward-looking aft port (two with 180 mm lenses, and the third camera affixed with an 85 mm lens), hence nearly doubling the field of view. This wide field of view offered the operators a view of the target aircraft well before it entered the two cameras with the narrow field of view and provided immediate feedback for instructing the pilots for the next pass. Each camera was upgraded from 8 to 32 GB of onboard RAM buffer; so, at full resolution and full speed, the record time increased from 0.8 to 3 s. These system improvements made successful recordings of the passing aircraft much easier and robust. In addition to the imaging platform improvements, the data acquisition system and cabling were modularized for easy installation and deinstallation. What took a week in the third campaign now takes approximately half a day.

The fourth flight campaign in December of 2018 was comprised of two flights. The first flight imaged a single T-38, the second flight imaged two T-38s flying in formation. The goal of the first flight was to image the shockwaves emanating from the lower surfaces of the plane. These shockwaves propagate to the ground, forming the classic N-wave that makes the sonic boom heard by people on the ground. The pilot must maneuver the aircraft into a 90 deg roll, known as a knife-edge view, as the plane passes below the observer plane. Figures 12, 13, 15, and 16 are from a pass from the third flight campaign in February of 2015, where the pilot attempted the 90 deg roll but made it too late to achieve the knife-edge view under the
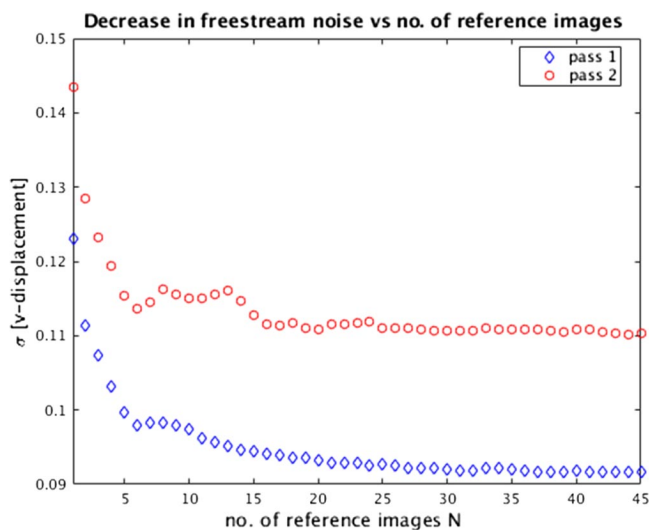

Fig. 14   Plot of rms of the noise in the optical flow solution with the number of reference images.
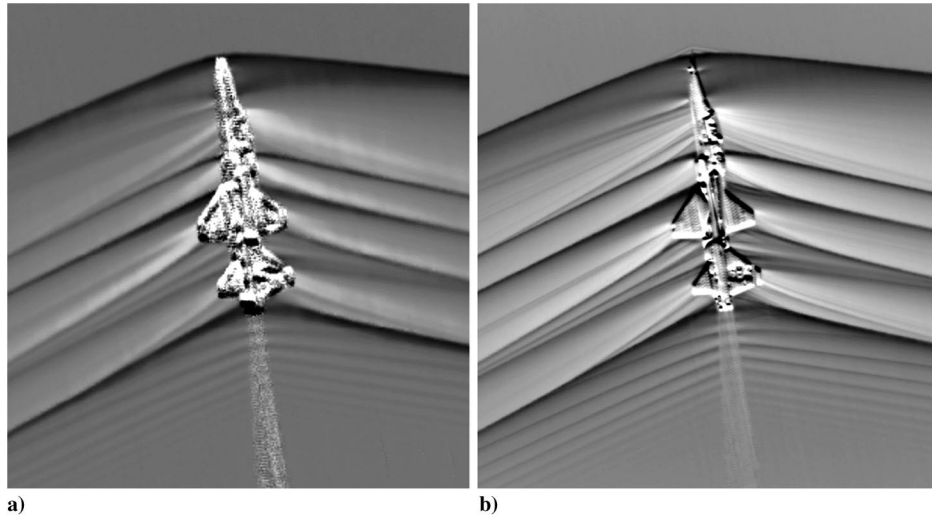
Fig. 16 **Comparison of solutions resulting from a) cross correlation and b) optimized Horn–Schunck optical flow algorithm. Rendering of the aircraft in the solution is the summation of random noise where it blocks the view of the background.**
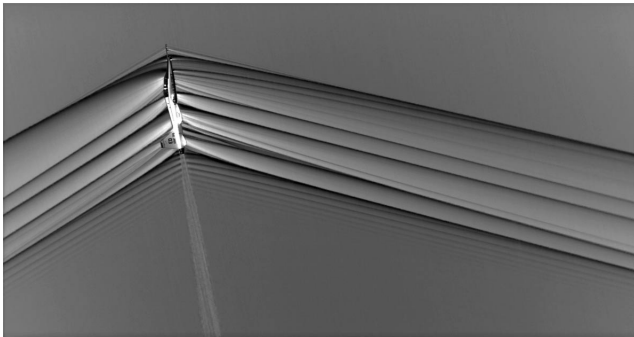

Fig. 17 **Contour of ± 2 pixels in the D_y direction of shock waves rendered by the optical flow routine of the T-38 at $M = 1.08$ in a knife-edge maneuver.**
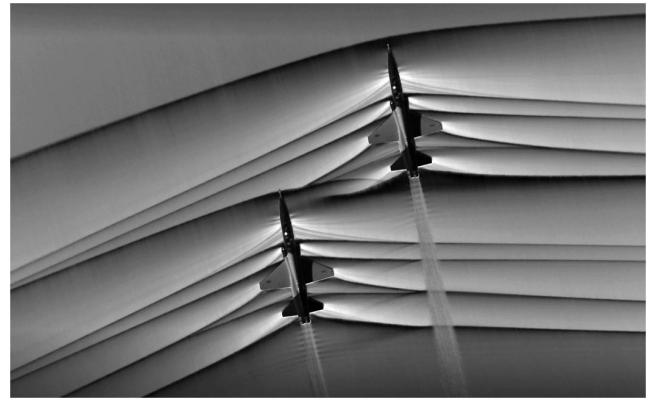

Fig. 19 **Contour of ± 2 pixels in the D_y direction of a formation of two T-38 aircraft at $M = 1.02$, flying one wingspan apart.**
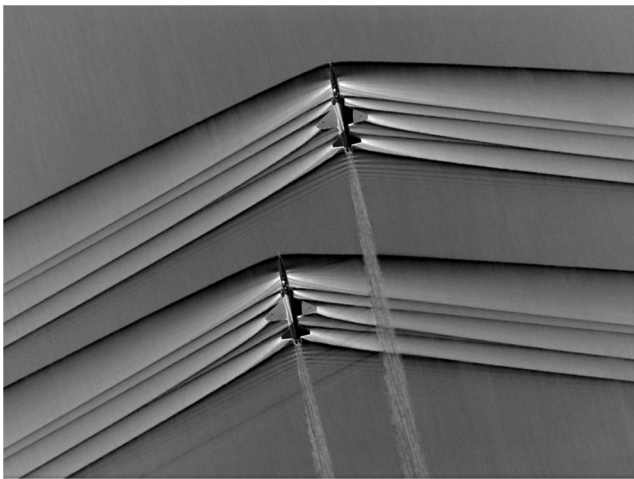

Fig. 18 **Contour of ± 2 pixels in the D_y direction of two T-38 aircraft flying at $M = 1.05$ with the shock structure of the trailing craft interacting with the plume only.**
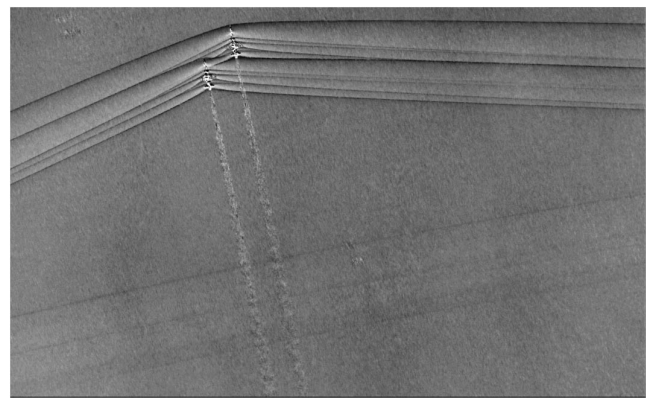

Fig. 20 **Contour of ± 2 pixels in the D_y direction of single frame from wide-angle camera showing the refracted shock structure propagating vertically from the Earth boundary layer.**

observer plane. Figure 17 shows the T-38 in the knife edge view during a pass in the first flight of the fourth flight campaign. Note the distinct difference of the lower surface shockwave pattern from the upper surface pattern.

Flight 4 from the fourth campaign concentrated on two-plane formation flights. The goal was to capture the shock wave interactions of the trailing aircraft with the other aircraft's tail shock and exhaust plume. The X-59 Low-Boom Flight Demonstrator is

configured with a horizontal tail near the top of the vertical stabilizer, generating a shock that propagates downward, and thus interacting with the engine exhaust plume. Concerns arose over this interaction, and so both wind-tunnel testing and computational modeling were performed [29,30]. Figure 18 shows results from a pass where two aircraft are far enough apart that the shock structure of the trailing craft had no interactions with the shocks of the lead craft. Note the reflection of the shocks off the plume throughout the shock structure.

Figure 19 shows the two aircraft flying one wingspan apart, with 10 ft of vertical separation, flying at $M = 1.01$. Note the bow shock of the trailing craft was distorted and eventually merged with the tail shock of the lead craft.

Figure 20 is a single data frame processed using 10 references to show, in addition to the near-field shock structure, the coalesced bow and tail shocks of the two aircraft become normal at a distance behind and below the aircraft. This occurs because with reducing altitude, the air temperature increases, the local speed of sound increases, and thus the local Mach number decreases. Eventually, the shock waves reduce to $M = 1.0$ and then refract back up into the atmosphere.

These data are derived from the wide-angle field of view offered by the third camera added for the AIRBOS4 campaign. Note the bow shock from the trailing T-38 merged with the tail shock of the lead. The refracted shock downstream for the two aircraft shows as three distinct straight lines.

VIII.   Conclusions

A new method for obtaining high-resolution imaging of density gradients in air around a full-scale airplane in flight has been demonstrated. The advantage of acquiring in-flight schlieren is that the data are of the true flight Reynolds condition, have nearly turbulence-free inflow, and have wide fields of view that capture flow phenomena that cannot occur in a wind tunnel. The utility of this technique goes beyond the capturing of shock waves; it can be used to study subsonic flows from tip vortices to propeller and helicopter blade-tip vortices. The ability to average the flowfield solutions of many instantaneous images improves the signal to noise such that the calculation of density from these data becomes more feasible. A modularized data acquisition system facilitates rapid installation in the observer aircraft, and optimized processing algorithms and computers make this overall method robust and efficient.

Acknowledgments

References

[1] Settles, G. S., *Schlieren and Shadowgraph Techniques, Visualizing Phenomena in Transparent Media*, 1st ed., Springer-Verlag, Berlin, 2001.

[2] Dalziel, S. B., Hughes, G. O., and Sutherland, B. R., "Whole Field Density Measurements by 'Synthetic Schlieren'," *Experiments in Fluids*, Vol. 28, No. 4, 2000, pp. 322–335.
https://doi.org/10.1007/s003480050391

[3] Richard, H., and Raffel, M., "Principle and Applications of the Background Oriented Schlieren (BOS) Method," *Measurement Science and Technology*, Vol. 12, No. 9, 2001, pp. 1576–1585.
https://doi.org/10.1088/0957-0233/12/9/325

[4] Raffel, M., Tung, C., Richard, H., Yu, Y., and Meier, G., "Background Oriented Stereoscopic Schlieren (BOSS) for Full Scale Helicopter Vortex Characterization," *Proceeding of the 9th International Symposium on Flow Visualization*, edited by G. M. Carlomango, Paper 450, Scotland, U.K., Aug. 2000.

[5] Weinstein, L. M., "An Optical Technique for Examining Aircraft Shock Wave Structures in Flight," NASA CP 3279, 1994, pp. 1–17.

[6] Hill, M. A., and Hearing, E. A., Jr., "Ground to Air Flow Visualization Using Solar Calcium-K Line Background Oriented Schlieren," *Experiments in Fluids*, Vol. 58, No. 1, 2017, Paper 4.
https://doi.org/10.1007/s00348-016-2285-7

[7] Banks, D. W., Heineck, J. T., Bean, P. S., Martin, B. J., Larson, D. N., Schairer, E. T., and Walker, L. A., "Flight Validation of an Air-to-Air Background Oriented Schlieren Technique," NASA TM-2014-218323, Oct. 2014.

[8] Kindler, K., Goldhahn, E., Leopold, F., and Raffel, M., "Recent Developments in Background Oriented Schlieren Methods for Rotor Blade Tip Vortex Measurements," *Experiments in Fluids*, Vol. 43, Nos. 2–3, 2007, pp. 233–240.
https://doi.org/10.1007/s00348-007-0328-9

[9] Bauknecht, A., Merz, C. B., Raffel, M., Landolt, A., and Meier, A. H., "Blade Tip Vortex Detection in Maneuvering Flight Using the Background Oriented Schlieren (BOS) Technique," *Journal of Aircraft*, Vol. 51, No. 6, 2014, pp. 2005–2014.
https://doi.org/10.2514/1.C032672

[10] Raffel, M., Heineck, J. T., Schairer, E. T., Leopold, F., and Kindler, K., "Background Oriented Schlieren Imaging for Full-Scale and In-Flight Testing," *Journal of the American Helicopter Society*, Vol. 59, No. 1, 2014, pp. 1–9.
https://doi.org/10.4050/JAHS.59.012002

[11] Raffel, M., "Background-Oriented Schlieren Techniques," *Experiments in Fluids*, Vol. 56, No. 3, 2015, Paper 60.
https://doi.org/10.1007/s00348-015-1927-5

[12] Venkatakrishnan, L., and Meier, G. E. A., "Density Measurements Using the Background Oriented Schlieren Technique," *Experiments in Fluids*, Vol. 37, No. 2, 2004, pp. 237–247.
https://doi.org/10.1007/s00348-004-0807-1

[13] Ihrke, I., and Magnor, M., "Image-Based Tomographic Reconstruction of Flames," *Proceedings of Eurographics/ACM SIGGRAPH Symposium on Computer Animation*, edited by R. Boulic, and D. K. Pai, 2004, pp. 367–375.

[14] Venkatakrishnan, L., "Density Measurements in an Axisymmetric Underexpanded Jet by Background-Oriented Schlieren Technique," *AIAA Journal*, Vol. 43, No. 7, 2005, pp. 1574–1579.
https://doi.org/10.2514/1.12647

[15] Goldhahn, E., and Seume, J., "The Background Oriented Schlieren Technique: Sensitivity, Accuracy, Resolution and Application to a Three-Dimensional Density Field," *Experiments in Fluids*, Vol. 43, Nos. 2–3, 2007, pp. 241–249.
https://doi.org/10.1007/s00348-007-0331-1

[16] Atcheson, B., Ihrke, I., and Heidrich, W., "Time-Resolved 3D Capture of Non-Stationary Gas Flows," *ACM Transactions on Graphics (Proceedings of SIGGRAPH Asia)*, Vol. 27, No. 5, Dec. 2008, Paper 132.
https://doi.org/10.1145/1457515.1409085

[17] Sourgen, F., Leopold, F., and Klatt, D., "Reconstruction of the Density Field Using the Colored Background Oriented Schlieren Technique (CBOS)," *Optics and Lasers in Engineering*, Vol. 50, No. 1, 2012, pp. 29–38.
https://doi.org/10.1016/j.optlaseng.2011.07.012

[18] Nicolas, F., Todoroff, V., Plyer, A., Le Besnerais, G., Donjat, D., Micheli, F., Champagnat, F., Cornic, P., and Le Sant, Y., "A Direct Approach for Instantaneous 3D Density Field Reconstruction from Background–Oriented Schlieren (BOS) Measurements," *Experiments in Fluids*, Vol. 57, No. 1, 2016, Paper 13.
https://doi.org/10.1007/s00348-015-2100-x

[19] Brown, C. A., Clem, M. M., and Fagan, A. F., "Investigation of Broadband Shock Noise from a Jet near a Planar Surface," *Journal of Aircraft*, Vol. 52, No. 1, 2015, pp. 266–273.
https://doi.org/10.2514/1.C032695

[20] Geerts, J. S., and Yu, K. H., "Systematic Application of Background-Oriented Schlieren for Isolator Shock Train Visualization," *AIAA Journal*, Vol. 55, No. 4, April 2017, pp. 1105–1117.
https://doi.org/10.2514/1.J054991

[21] Heineck, J. T., Schairer, E. T., Walker, L. A., and Kushner, L. K., "Retroreflective Background Oriented Schlieren (RBOS)," *14th International Symposium on Flow Visualization*, June 2010.

[22] "USDA Plant Website," http://plants.usda.gov/core/profile?symbol=LATR2 [retrieved 15 March 2011].

[23] "Vision Research, Inc. Website," https://www.phantomhighspeed.com/products/cameras/veo/veo640 [retrieved 24 April 2016].

[24] Hargather, M. J., and Settles, G. S., "Natural-Background-Oriented Schlieren Imaging," *Experiments in Fluids*, Vol. 48, No. 1, 2010, pp. 59–68.
https://doi.org/10.1007/s00348-009-0709-3

[25] Lucas, B. D., and Kanade, T., "An Iterative Image Registration Technique with an Application to Stereo Vision," *Proceedings of the 7th International Joint Conference on Artificial Intelligence (IJCAI'81)*, Vol. 2, Morgan Kaufmann, San Francisco, CA, 1981, pp. 674–679.
https://doi.org/10.5555/1623264.1623280

[26] Atcheson, B., Heidrich, W., and Ihrke, I., "An Evaluation of Optical Flow Algorithms for Background Oriented Schlieren Imaging," *Experiments in Fluids*, Vol. 46, No. 3, 2009, pp. 467–476.
https://doi.org/10.1007/s00348-008-0572-7

[27] Smith, N. T., Heineck, J. T., and Schairer, E. T., "Optical Flow for Flight and Wind Tunnel Background Oriented Schlieren Imaging," *AIAA Science and Technology Forum*, AIAA Paper 2017-0472, Jan. 2017.
https://doi.org/10.2514/6.2017-0472

[28] Horn, B., and Schunck, B., "Determining Optical Flow," *Artificial Intelligence*, Vol. 17, Nos. 1–3, 1981, pp. 185–203.
https://doi.org/10.1016/0004-3702(81)90024-2

[29] Castner, R., "Exhaust Nozzle Plume Effects on Sonic Boom," *Journal of Aircraft*, Vol. 49, No. 2, March–April 2012, pp. 415–422.
https://doi.org/10.2514/1.C031305

[30] Durston, D. A., Cliff, S. E., Denison, M. F., Jensen, J. C., Moran, P. J., Smith, N. T., Heineck, J. T., Schairer, E. T., Kushner, L. K., and Castner, R. S., "Nozzle Plume/Shock Interaction Experimental and Computational Sonic Boom Analyses from the NASA Ames 9- by 7-Foot Supersonic Wind Tunnel," NASA TP-2018-219879, 2018.

L. Ukeiley
Associate Editor